Three-Dimensional Conjugate CFD Simulations of Internal Window Frame Cavities Validated Using IR Thermography

Arild Gustavsen

Brent T. Griffith
Student Member ASHRAE

Dariush Arasteh, P.E.
Member ASHRAE

ABSTRACT

This paper studies the effectiveness of one commercial computational fluid dynamics (CFD) program for simulating combined natural convection and heat transfer in three dimensions for air-filled cavities similar to those found in the extruded frame sections of windows. The accuracy of the conjugate CFD simulations is evaluated by comparing results for surface temperature on the warm side of the specimens to results from experiments that use infrared (IR) thermography to map surface temperatures during steady-state thermal tests between ambient thermal chambers set at 0ºC and 20ºC. Validations using surface temperatures have been used in previous studies of two-dimensional simulations of glazing cavities with generally good results. Using the techniques presented and a noncontact infrared scanning radiometer we obtained surface temperature maps with a resolution of 0.1ºC and 3 mm and an estimated uncertainty of ±0.5ºC and ±3 mm. Simulation results are compared to temperature line and contour plots for the warm side of the specimen. Six different cases were studied, including a simple square section in a single vertical cavity and two four-sided frame cavities as well as more complex H- and U-shaped sections. The conjugate CFD simulations modeled the enclosed air cavities, the frame section walls, and the foam board surround panel. Boundary conditions at the indoor and outdoor air/solid interface were modeled using constant surface heat-transfer coefficients with fixed ambient-air temperatures. In general, there was good agreement between the simulations and experiments, although the accuracy of the simulations is not explicitly quantified. We conclude that such simulations are useful for future evaluations of natural convection heat transfer in frame cavities.

INTRODUCTION

Considerable research effort has been made during recent decades on improving calculation and measurement procedures for predicting the thermal performance of building envelope components such as windows, doors, and walls (ElSherbiny et al. 1982; Wright and Sullivan 1994; Shewen et al. 1996; Griffith et al. 1998; Carpenter and McGowan 1998; Larsson et al. 1999). This research has resulted in some standardized methods of measuring and calculating the thermal performance of building components and in new computer simulation programs that can be used on a routine basis (Finlayson et al. 1998; EE 1995). These computer programs can often substitute for more expensive experiments; however, to be sure that these programs accurately predict thermal properties, it is necessary to validate them using results from physical tests and research simulations.

Historically, the thermal performance parameter of interest has been the thermal transmittance or U-factor because it is used to size the loads that a building heating and cooling system must address. Thus, the traditional method of verifying computer programs is to compare calculated U-factors with measured values. This way of validating the computer programs makes use of one single aggregate parameter (total heat flow) and, therefore, does not offer scientists sufficient detail to verify that calculations are correct. Relying only on the thermal transmittance coefficient means that temperature gradients on the surface of the specimen are not taken into account.

Another way of verifying the accuracy of computer simulations of heat transfer is to compare them to measured results for surface temperature. Using infrared (IR) thermography allows the researchers to gather many temperature data for the

Arild Gustavsen is a university lecturer in the Department of Building and Construction, Norwegian University of Science and Technology, Trondheim, Norway. **Brent T. Griffith** is a graduate student research assistant at Massachusetts Institute of Technology, Cambridge, Mass. **Dariush Arasteh** is a staff scientist at Lawrence Berkeley National Laboratory, Berkeley, Calif.

TABLE 1
Specimen Descriptions

Description	1-inch square frame	2-inch square frame	Vertical 2-inch section	Vertical 2-inch H-section	Vertical 2-inch U-section	Horizontal 2-inch U-section
Orientation during test	entire frame	entire frame	vertical	vertical	vertical	horizontal
Overall height (mm)	800	800	800	640	580	49.8
Overall width (mm)	800	800	50.8	49.8	49.8	580
Outer size of cross-section (mm)	25.4	50.8	50.8	49.8	49.8	49.8
Outer depth of frame section (mm)	25.4	50.8	50.8	48.4	50.8	50.8
Wall thickness (mm)	2.0	2.0	2.0	2.0	2.0	2.0
Size of inner cavity (maximum length in heat flow direction) (mm)	21.4	46.8	46.8	44.4	46.8	46.8
H/L aspect ratio	37.2/1	17.0/1	17.1	14.4	12.4	0.98
W/L aspect ratio	1/37.2	1/17.0	1	N/A	N/A	N/A
Maximum Rayleigh number, Ra_{max}	2.4×10^4	2.5×10^5	2.5×10^5	2.2×10^5	2.5×10^5	2.5×10^5

surface of a specimen. Scientists using the traditional approach could use thermocouples to gather temperature data, but this approach does not give temperature data with the high spatial resolution of infrared thermography data. Both the U-factors and the infrared thermography approaches have been used previously to verify computer codes and computer simulations (Carpenter and Elmahdy 1994; Sullivan et al. 1996; Griffith et al. 1998).

In this study we assess the usefulness of a commercially available computational fluid dynamics (CFD) computer program for simulating geometries typically found in buildings, such as window frames with internal cavities (e.g., aluminum and vinyl frame sections). The simulations modeled combine fluid flow and heat transfer in three dimensions inside cavities similar to those found in a vinyl frame section. A previous investigation of conjugate CFD models that compared results for two-dimensional models of glazing cavities to infrared thermographic measurements showed generally good agreement (Sullivan et al. 1996). Both in that study and in the current one, conjugate CFD techniques were used to model an enclosed air cavity, and the warm side and cold side surfaces were modeled using constant heat-transfer coefficients and a fixed ambient air temperature. Measured data were collected using infrared thermography to map surface temperatures on the warm side of specimens during steady-state thermal tests between 0ºC and 20ºC.

SPECIMENS

Six different frame cavity specimens were measured and modeled. Although each specimen can be thought of as either a complete window frame or a component of a complete window frame, the sections used were not actual window

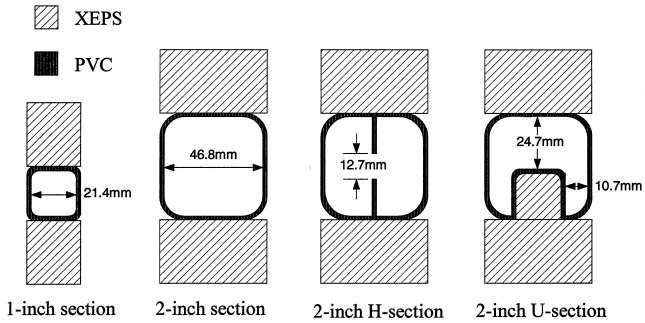

Figure 1 *Schematic of cross sections for one-inch, two-inch, two-inch H, and two-inch U-section specimens.*

frames but rather standard and custom vinyl extrusions. The sizes of the profiles in cross section were chosen to span the range of internal cavity sizes generally found in window frames. The simple shapes of the profiles were chosen to limit the complexity of the CFD model and to allow us to better understand the natural convection effects found in the experiments and simulations. Because the maximum reasonable size of a specimen that can be tested in the Infrared Thermography Laboratory (IR Lab) is approximately 0.9 m by 0.9 m, we used specimens with a maximum area of 0.8 m by 0.8 m. This size limitation helped to ensure homogenous boundary conditions across the full width of the specimen. Polyvinyl chloride (PVC) was used to form the cavities so that larger temperature gradients could develop on the surface compared

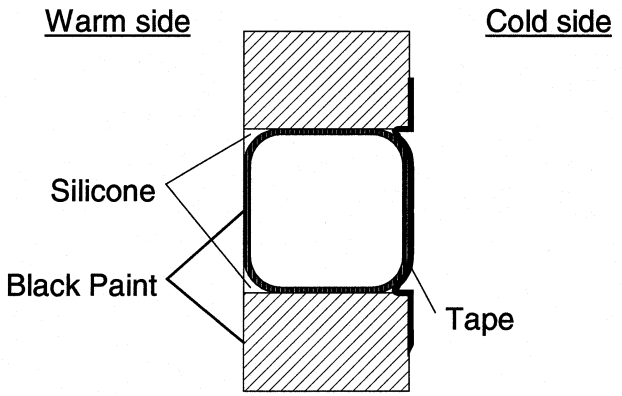

Figure 2 *Schematic of air-sealing techniques for thermal testing.*

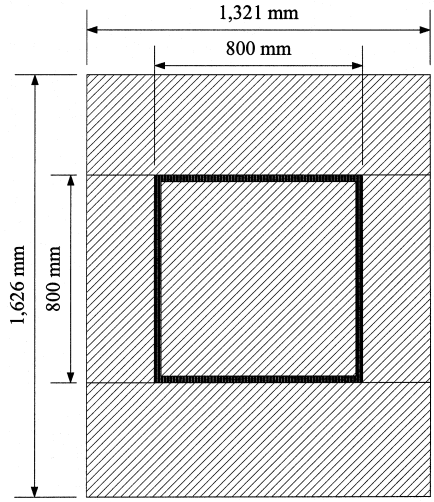

Figure 3 *Mounting of entire frame specimen in the XEPS surround panel; the figure is drawn for the dimensions of the one-inch square frame specimen.*

to those that would be found with a more highly conductive frame material such as aluminum.

The specimens are listed in Table 1 along with their dimensions and testing orientation. The Rayleigh numbers listed in Table 1 are maximums that were calculated based on the size of the inner cavity for the extreme case where the temperature difference is 20ºC. Figure 1 diagrams the cross sections of the different frame geometries; from left to right we see the one-inch section, two-inch section, the two-inch H-section and the two-inch U-section.

Specimen Mounting

The specimens were mounted in foam board surround panels for thermal testing. The CFD simulation focused on only the frame cavities, so the mounting was designed to match the boundary conditions of the model rather than the configuration found in a real window. The one-inch specimen

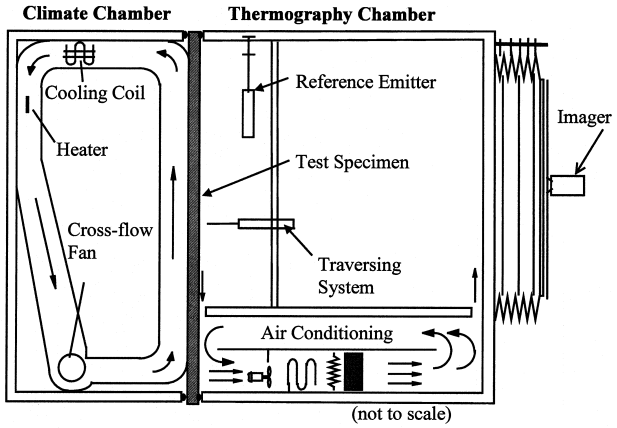

Figure 4 *Figure of IR box used to generate steady-state heat flow through test specimen.*

was mounted in 25.4-mm-thick extruded polystyrene (XEPS) foam board, and the two-inch-thick specimens were mounted in 50.8-mm-thick XEPS. Figure 2 shows how the frame sections were sealed to the surround panel to eliminate air infiltration. On the warm side of the test specimen, the small cavity created by the rounded edge of the frame section was filled with silicone sealant to make the surface flat. On the cold side, the joint was sealed using pressure-sensitive vinyl tape that was carefully applied to limit pockets of trapped air. The square frames were assembled much like complete window frames with a continuous air cavity around all four sides, as shown in Figure 3. Instead of a glazing unit, the frames were filled with XEPS of the same thickness as the profiles themselves. The area covered by each frame was 0.8 m by 0.8 m. For the three vertical tests, single lengths of a frame section were mounted vertically so that the long axis of the cavity was oriented parallel to gravity and perpendicular to heat flow. For the horizontal test, a single length of the frame section was mounted horizontally so that the long axis of the cavity was oriented perpendicular to gravity and perpendicular to heat flow. The warm-side surface of each specimen was painted to ensure a uniform surface emittance of 0.9. Location markers (thin aluminum strips, 3 mm by 50 mm) were attached to the surface of the surround panel to allow us to identify locations in the infrared images so we could relate image pixels to spatial coordinates.

EXPERIMENTS

Thermal testing gathered measured data to compare to the results of simulations. Infrared thermography was used because this technique can collect, in a non-invasive fashion, surface temperature data with high spatial resolution. The equipment and procedures used to conduct these measurements at the IR Lab have previously been described in the literature (Griffith and Arasteh 1999; Türler et al. 1997; Griffith et al. 1995). A summary is provided here for completeness.

IR Box

The main apparatus used in the IR Lab for thermal testing is the IR box, which generates steady-state heat flow through the test specimen. A specimen is mounted between a warm chamber (the thermography chamber) and a climate chamber, as shown in Figure 4. The climate chamber is used to simulate cold outdoor conditions, and the thermography chamber simulates normal indoor conditions. The IR box is similar to an ordinary hot box used to measure U-factor (described in ISO 1994) except that there is no baffle in the thermography chamber. The baffle is removed so the IR imager can have a full view of the test specimen. The opening between the climate chamber and the thermography chamber is 1.2 m by 1.2 m.

Thermal Conditions

In the climate chamber, the air flow is upward and parallel to the test specimen's surface, with a baffle placed 10 cm from the surface of the test specimen. The entire air flow is routed through ducts that have nearly constant cross-sectional size and rounded corners where the wind changes direction (see Figure 4). The absolute airspeed is about 3.0 m/s but depends on chamber operation and specimen geometry.

The thermography chamber allows an IR imager to measure the surface temperature of the specimen while air temperature and velocity are controlled and measured on the warm side of the specimen under uniform thermal radiation conditions. The thermography chamber's outer size is 1.4 m wide and 2.1 m high. The depth can vary from 0.9 to 4.2 m; bellows is used to vary the depth of the chamber, and the full depth is used to capture a full-size image of a test specimen. Air circulation is controlled in a recirculation zone within the chamber subfloor. A 50-mm-wide slot runs across the entire width of the subfloor at the edge beneath the specimen, creating an air sink that drains cooler air running off the specimen into the subfloor. At the opposite edge of the subfloor, a 40-mm-wide output slot introduces conditioned air at low velocity to the warm chamber.

During our experiments, we used ISO conditions (ISO 1998); the bulk air temperature of the warm side was controlled at 20ºC, and the cold-side bulk air temperature was controlled at 0ºC. Separate experiments were performed to characterize the performance of the IR box for the rates of surface heat transfer. A special test specimen, known as a calibrated transfer standard (CTS), was used to directly measure the rates of surface heat transfer or film coefficients. Although the exact film coefficients during a given test depend on the specimen, the CTS technique has been adopted to characterize and adjust the operation of a specific thermal test facility (ASTM 1199). A CTS is a large-area heat flux transducer that consists of two sheets of glass sandwiching an expanded polystyrene (EPS) foam core. The CTS used here measures 914 mm high by 610 mm wide and 23.1 mm thick. It is instrumented with 12 pairs of thermocouples situated at the interface between foam and glass that are used to measure the temperature difference across the foam. The thermal conductivity of the foam is characterized separately so that the total heat flow through the specimen can be determined. From the total heat flow and the conductivity of the glass, the surface temperatures at the interfaces between glass and air are determined. Overall surface heat transfer coefficients are then determined using averaged values for surface temperatures, the total heat flow, and the bulk air temperatures. See the test method (ASTM 1199) for a more complete description of the data reduction methods. The overall surface heat-transfer coefficient for the cold side was measured at 26±5 W/m^2 K. The overall surface heat-transfer coefficient for the warm side was measured at 7.9±0.4 W/m^2 K.

Data Acquisition

The environmental chambers are controlled and monitored by a computer-based data acquisition system. Data noted include air temperature and velocity, specimen surface temperature, and relative humidity. These data are used to ensure stable environmental conditions. The computer-based system can also be used to measure the surface temperature in the more traditional way by means of thermocouples attached directly to the specimen. This added measurement technique is useful for measuring the temperature on the back side of the specimen (the side of the specimen facing the climate chamber) and also to verify the thermal imaging results. A traversing system can be used for measurement of air temperature and velocity.

Infrared Measurements

The thermal imager captures test specimen surface temperature data on the warm side of the specimen and is mounted either inside or outside the chamber. A typical measurement setup is shown in Figure 5. A reference emitter and a background mirror are used to achieve uncertainties of

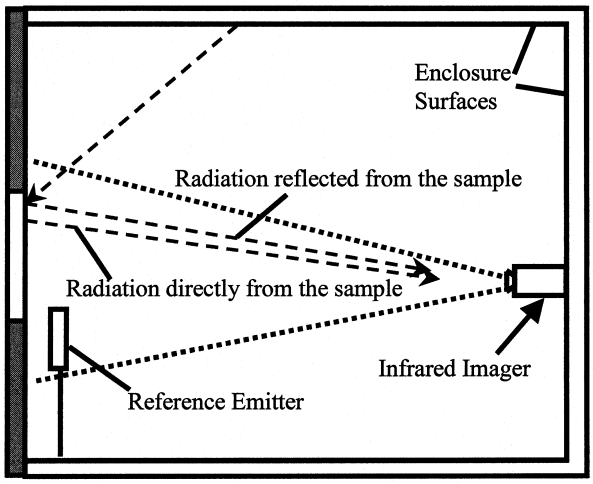

Figure 5 *A typical thermography setup.*

about ±0.5°C (Griffith and Arasteh 1999). The measurement and calculation procedures are described below.

Determining Surface Emissivity

The emissivity of the samples being measured is important in IR thermography because it has a direct bearing on the strength and spectral distribution of radiation leaving the surface, which is the item being measured and, in turn, being interpreted to estimate surface temperature. Emissivity values found in standard tables are not employed because they might be different from the value found within the spectral range of the imager. Thus, the emissivity of a sample is measured in a separate experiment in which the sample is compared to another material with a known emissivity, e_{ref}. Thin samples from both materials are mounted on an isothermal plate that has a temperature 10°C to 20°C above or below the background temperature to ensure high contrast between the radiation from the specimens and from the background. Next, the background compensation in the infrared imager software (Bales 1993) is turned off by setting the emissivity to 1.0. Both samples are then imaged simultaneously. Readings are averaged both over time and space to find the equivalent blackbody temperature of the sample, $T_{e=1,smpl}$ (K), and the equivalent blackbody temperature of the known reference material, $T_{e=1,ref}$ (K). Also, an equivalent blackbody temperature, T_{back} (K), for the background environment is found by using a background mirror (which reflects the background radiation). The emissivity of the sample, e_{smpl}, is then calculated from (Griffith and Arasteh 1999)

$$e_{smpl} = \frac{T^4_{e=1,\,smpl} - T^4_{back}}{T^4_{e=1,\,ref} - T^4_{back}} \cdot e_{ref} \,. \tag{1}$$

Determining the Infrared Temperature

The temperature of the specimen is found by averaging a number of consecutive IR images, usually 16, giving us $T_{e=1}$ (K). The subscript $e = 1$ is a result of setting the emissivity to 1 in the thermography software before taking the images. Each image can consist of 1,024 by 768 data points (the usual resolution is about 500 by 500), and each point represents the temperature of a given point on the surface of the test specimen. Two types of views are possible: close-ups showing only parts of the specimen in the picture and complete shots with the entire specimen in one picture. Once the specimen has been measured, we attach a background mirror to it and capture and average a new set of 16 images, giving us T_{back} (K) (still with the emissivity set to 1). The background mirror is used to correct the previously measured temperature for background radiation. The mirror is kept small to lessen the effect of reduced surface emissivity on the overall thermal situation. From the above procedure we calculate the infrared specimen temperature T_{IR} (K) (Türler et al. 1997),

$$T_{IR} = \left(\frac{T^4_{e=1} - (1 - e_{surf}) \cdot T^4_{back}}{e_{surf}} \right)^{1/4} \tag{2}$$

where e_{surf} is the previously measured emissivity of the sample. If the camera had been perfectly calibrated and no drift was expected with time, T_{IR} could be the final result. However, the uncertainty of using the above approach is normally ±2°C; therefore, we use a reference emitter to increase our accuracy (see next paragraph). The IR temperature can be calculated point by point (using values of T_{back} and $T_{e=1}$ from the same location) or by using a mean value of the background temperature T_{back} for the entire sample. The type of approach used is determined by the complexity of the specimen surface.

Correcting the Infrared Temperature Using a Reference Emitter

To correct for drift and uncertainties in the infrared imager, we use a reference emitter. The reference emitter is a temperature-controlled device with a known surface emissivity. During each measurement, the reference emitter is situated near the specimen being measured and within the field of view of the infrared imager. The reference emitter is kept relatively in focus while the imager is focused on the test specimen. The infrared temperature of the reference emitter $T_{IR,ref}$ is compared to a direct contact measurement $T_{DC,\,ref}$ and the deviation is used to scale the infrared results for the test specimen $T_{IR,smpl}$ to find the temperature T:

$$T = T_{IR,\,sampl} - (T_{IR,\,ref} - T_{DC,\,ref}) \tag{3}$$

The reference emitter is designed and placed so that its presence interferes minimally with air temperature and flow along the specimen.

NUMERICAL CALCULATIONS

A commercial computational fluid dynamics (CFD) program was used for the numerical part of this study (Fluent 1998). This program is for modeling fluid flow and heat transfer in complex geometries and uses a control-volume-based technique to solve the governing equations.

Mathematical Model

The governing equations for the system can be written using different notations. Here, we write the equations for a transient, three-dimensional, and incompressible problem. In Table 1 we see that the maximum Rayleigh number, Ra_{max}, for the vertical, one-inch section is close to the laminar/turbulence limit. Flow changes from laminar to turbulent near $Ra = 2 \times 10^4$ for two-dimensional cavities where $H/L = 40$ (Yin et al. 1978). However, the temperature difference between the internal walls of the cavity is likely to be smaller than 20°C, which is the temperature difference used for calculating the maximum Rayleigh number, so the real Rayleigh number is lower. In addition, the turbulence limit is probably

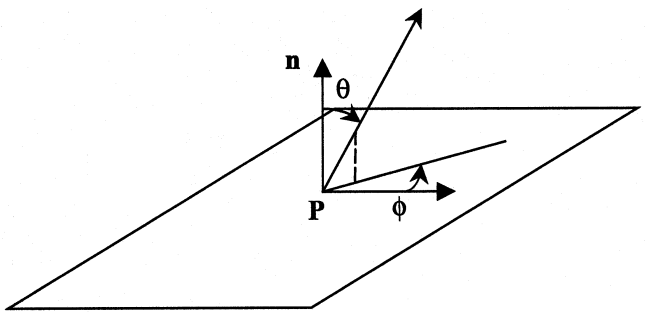

Figure 6 *Angles θ and ϕ define the hemispherical solid angle about a point P on a boundary face.*

higher (above Ra = 2×10^4) for a three-dimensional vertical square cavity than for a two-dimensional cavity because of the added restriction imposed on the flow by the narrowness of the cavity. We therefore assume laminar flow. Further we omit viscous dissipation and only consider transport of one gas, air. We assume that all air properties are constant (that is, the conductivity k, specific heat capacity c_p, and dynamic viscosity μ are constant). We also assume that the density ρ is constant, except in the buoyancy term in the y-momentum equation where we use the Boussinesq approximation. The equation for conservation mass can be written as

$$\frac{\partial \rho}{\partial t} + \frac{\partial}{\partial x}(\rho u) + \frac{\partial}{\partial y}(\rho v) + \frac{\partial}{\partial z}(\rho w) = 0 \tag{4}$$

where u, v, and w are the velocities in the x, y, and z directions, respectively, and t is the time variable. The momentum equations take the following form:

$$\begin{aligned} &\frac{\partial u}{\partial t} + \frac{\partial}{\partial x}(\rho uu) + \frac{\partial}{\partial y}(\rho vu) + \frac{\partial}{\partial z}(\rho wu) \\ &= -\frac{\partial p}{\partial x} + \frac{\partial}{\partial x}\left(\mu \frac{\partial u}{\partial x}\right) + \frac{\partial}{\partial y}\left(\mu \frac{\partial u}{\partial y}\right) + \frac{\partial}{\partial z}\left(\mu \frac{\partial u}{\partial z}\right) \end{aligned} \tag{5}$$

$$\begin{aligned} &\frac{\partial u}{\partial t} + \frac{\partial}{\partial x}(\rho uv) + \frac{\partial}{\partial y}(\rho vv) + \frac{\partial}{\partial z}(\rho wv) \\ &= -\frac{\partial p}{\partial y} + \frac{\partial}{\partial x}\left(\mu \frac{\partial v}{\partial x}\right) + \frac{\partial}{\partial y}\left(\mu \frac{\partial v}{\partial y}\right) + \frac{\partial}{\partial z}\left(\mu \frac{\partial v}{\partial z}\right) - \rho g \beta (T - T_r) \end{aligned} \tag{6}$$

$$\begin{aligned} &\frac{\partial u}{\partial t} + \frac{\partial}{\partial x}(\rho uw) + \frac{\partial}{\partial y}(\rho vw) + \frac{\partial}{\partial z}(\rho ww) \\ &= -\frac{\partial p}{\partial z} + \frac{\partial}{\partial x}\left(\mu \frac{\partial w}{\partial x}\right) + \frac{\partial}{\partial y}\left(\mu \frac{\partial w}{\partial y}\right) + \frac{\partial}{\partial z}\left(\mu \frac{\partial w}{\partial z}\right) \end{aligned} \tag{7}$$

for the x, y, and z directions, respectively. We calculate the buoyancy (or thermal expansion) coefficient β from $\beta = 1/T_m$; g is gravity in the y direction, and p is static pressure. The expression for thermal expansion coefficient β is based on the perfect gas assumption. The energy equation can be written

$$\begin{aligned} &\rho c_p \frac{\partial T}{\partial t} + \rho c_p \frac{\partial}{\partial x}(uT) + \rho c_p \frac{\partial}{\partial y}(vT) + \rho c_p \frac{\partial}{\partial z}(wT) \\ &= \frac{\partial}{\partial x}\left(k \frac{\partial T}{\partial x}\right) + \frac{\partial}{\partial y}\left(k \frac{\partial T}{\partial y}\right) + \frac{\partial}{\partial z}\left(k \frac{\partial T}{\partial z}\right) + S_h . \end{aligned} \tag{8}$$

T is the air temperature, and S_h is an energy source that can be a result of radiation. In solid regions, the CFD program calculates conductive heat transfer from

$$\rho c_p \frac{\partial T}{\partial t} = \frac{\partial}{\partial x}\left(k \frac{\partial T}{\partial x}\right) + \frac{\partial}{\partial y}\left(k \frac{\partial T}{\partial y}\right) + \frac{\partial}{\partial z}\left(k \frac{\partial T}{\partial z}\right) + q''' . \tag{9}$$

We use the discrete transfer radiation model (DTRM) to calculate radiant heat transfer inside the internal air cavities. This model assumes that a single ray can approximate the radiation leaving a surface element in a certain range of solid angles (see Figure 6) and that the surfaces are diffuse gray. The accuracy of the model is mainly limited by the number of rays traced and the computational grid. At each radiation face, rays are fired at discrete values of the zenith and azimuth angles. To cover the radiating hemisphere, θ and ϕ are varied from 0 to $\pi/2$ and 0 to 2π, respectively. Thus, the ray tracing technique used in DTRM can provide a prediction of radiant heat transfer between surfaces without the use of explicit view-factor calculations.

The radiation intensity approaching a point on a wall surface is integrated to yield the incident radiation heat flux q_{in} as

$$q_{in} = \int_{\boldsymbol{s} \cdot \boldsymbol{n} > 0} I_{in} \boldsymbol{s} \cdot \boldsymbol{n} d\Omega \tag{10}$$

where Ω is the hemispherical solid angle, I_{in} is the intensity of the incoming ray, $\boldsymbol{s}$ is the ray direction vector, and $\boldsymbol{n}$ is the normal pointing out of the domain. The net radiant heat flux from the surface q_{out} is computed as a sum of the reflected portion of q_{in} and the emissive power of the surface:

$$q_{out} = (1 - \varepsilon_w) q_{in} + \varepsilon_w \sigma T_w^4 \tag{11}$$

where T_w is the surface temperature of point **P** on the surface, and ε_w is the wall emissivity.

In our model we use three types of boundary conditions: the heat flux boundary condition (at adiabatic boundaries), the symmetry boundary condition, and the convective heat transfer boundary condition. The CFD program assumes zero flux of all quantities across a symmetry boundary. That is, there is no convective flux and no diffusive flux across a symmetry plane—the normal velocity component at the symmetry plane is zero and the normal gradients of all flow variables are zero at the symmetry plane. For the convective boundary condition, the heat flux to the wall is calculated from

$$q'' = h_f (T_w - T_f) + q''_{rad} = h_{ext} (T_{ext} - T_w) \tag{12}$$

where h_f and h_{ext} are the fluid and external (warm and cold sides) heat transfer coefficients; T_w, T_f, and T_{ext} are the wall,

TABLE 2
Material Properties Used in the Computer Simulations

Material	Emissivity	Thermal conductivity, (W/m-K)
PVC	0.9	0.17
Painted XEPS	0.9	0.03

fluid, and external heat sink temperatures; and q''_{rad} is the radiant heat flux.

Numerical Method

The CFD program uses a control-volume-based technique to convert the governing equations above to algebraic equations that can be solved numerically (Fluent 1998). The control-volume technique consists of integrating the governing equations about each control volume, which yields discrete equations that conserve each quantity on a control-volume basis. That is, the complete geometry is divided into small control volumes for which the discretized equations are solved. We used the program's segregated solver with double precision to solve the discretized equations. The segregated solver solves the different equations sequentially. After discretization, the conservation equation for a general variable ϕ at cell P can be written as

$$a_P \phi_P = \sum_{nb} a_{nb} \phi_{nb} + b \tag{13}$$

where the subscript nb refers to neighbor cells, a_P and a_{nb} are the linearized coefficients for ϕ_P and ϕ_{nb}, and b is the source term. These equations are solved using a Gauss-Seidel linear equation solver in conjunction with an algebraic multigrid method.

The discrete values are stored for the center of each cell. However, when solving the equations, we also need face values for the variables in the convection terms. For the energy and momentum variables, these are found by using the QUICK (quadratic upstream interpolation for convective kinetics) scheme. In addition the CFD program uses central differences to approximate the diffusion terms and SIMPLEC (semi-implicit method for pressure-linked equations consistent) to couple the interaction between pressure and velocity. The CFD program also has to use a pressure-interpolation scheme to find the pressure values at the cell faces. This is necessary because the program stores the pressure values in the cell centers just as it does for the rest of the variables. We chose to use the PRESTO (pressure staggering option) scheme, which is like the staggered grid approach described by Patankar (1980). The PRESTO scheme is recommended for buoyancy flows and hexahedral meshes. Because the equations are nonlinear, we use relaxation for some of the variables to avoid divergence.

Convergence is determined by checking the scaled residuals,

TABLE 3
Boundary Conditions Used in the Computer Simulations

Surface	Temperature (°C)	Total Surface Film Coefficient (W/m^2K)
Warm side	20	7.69
Cold side	0	25

$$R^{\phi} = \frac{\sum_{cells\ P} \left| \sum_{nb} a_{nb} \phi_{nb} + b - a_P \phi_P \right|}{\sum_{cells\ P} \left| a_P \phi_P \right|} \tag{14}$$

and ensuring that they are less than 10^{-5} for all variables except for the energy equation in which the residuals have to be less than 10^{-6}.

Material Properties and Boundary Conditions

The material properties and the boundary conditions used during the numerical simulations are shown in Tables 2 and 3. Air properties were calculated at 10°C. Surface film coefficients were selected from CEN (1998); note that these values are within the uncertainty ranges of the results obtained for the test chambers from measurements using a 13-mm foam core CTS.

MEASUREMENT AND SIMULATION CONSIDERATIONS

Because it is not practical to simulate every subtlety of the specimens, differences between the specimens and the computer models invariably arise. Characteristics of the experiments that were not directly modeled include the use of silicone to seal and flatten the warm-side surface, the presence of paint on the warm-side surface, and the use of vinyl tape on the cold side to form an air seal between the specimen and the surround panel. For the difference between the simulated and measured profiles, we also know that silicone has about the same conductivity as PVC.

In Figure 1 we see that the edges of the frame sections are round; however, in the simulations we used square, orthogonal angles at these edges. The effect of this simplification was tested in a separate two-dimensional simulation that compared models with rounded (as tested) and square edges. We found that the total heat transfer through the different configurations changed by 0.2% and that the surface temperature data deviated by a maximum of 0.4°C. The biggest difference in temperature was found right above the place were the simplification in edge shape was made. For the other places, the difference was much smaller.

Symmetry boundary conditions were also used where possible to reduce the number of computational cells and to reduce computation time. Such an assumption could lead to exclusion of particular effects or modification of the "real" solution, but, as we will see later, this approach does not seem

TABLE 4
Simulation Summary*

Description	Number of nodes	Energy residual	Momentum residual	Continuity residual
1-in. square frame	868,992	2.6532×10^{-9}	$1.7090>\times10^{-6}$	9.8472×10^{-6}
2-in. square frame	868,992	N/A	N/A	N/A
Vertical, 2-in. section	238,000	1.90×10^{-10}	$>4.28\times10^{-8}$	9.85×10^{-6}
Vertical, 2-in. H-section	310,320	1.27×10^{-10}	$>4.26\times10^{-8}$	9.99×10^{-6}
Vertical, 2-in. U-section	506,440	6.99×10^{-6}	$>3.86\times10^{-10}$	7.56×10^{-8}
Horizontal, 2-in. U-section	506,440	7.02×10^{-6}	$>4.18\times10^{-5}$	1.53×10^{-4}

* For the two-inch square frame we did not find a steady-state solution, and used a transient solution procedure.

to have introduced additional error. The "Results" section notes where the symmetry boundary condition was used.

SENSITIVITY OF NUMERICAL PROCEDURE AND GRIDDING

We chose a hexahedral mesh for discretization of the different geometries. To ensure that the resolution in the discretization of the geometry was high enough, some grid sensitivity tests were performed. Some of these were not performed on the final geometries but on simpler sections that represent one part of the more complex geometries. This approach was chosen to limit the simulation time (some of the complete sections took several days to simulate). One test was performed on a two-dimensional high-aspect-ratio cavity ($A = H/L = 40$) with two vertical isothermal walls separated by two horizontal adiabatic walls. We varied the grid density (using an equispaced grid, the same as used inside the air cavities in the frame models) both in the heat flow direction and in the vertical direction. We found that a mesh consisting of 25 nodes in the heat flow direction and 200 nodes in the vertical direction was sufficient. Further refinement only resulted in minor changes in the Nusselt number (a mesh with 45×450 nodes resulted in a change of Nusselt number by 1%). Using a mesh with 25×200 nodes within the vertical part of the one-inch-square frame also results in a grid aspect ratio of 4.4, which is less than the suggested maximum value of 5 (Fluent 1998). One test was also performed on a three-dimensional, horizontal, two-inch section. The number of nodes was increased both within the solid materials and in the air cavity. The refinement resulted in a change of only 0.3% in the total heat transfer through the test specimen. The boundary conditions in this test were identical to the boundary conditions in the final simulations. We also tried to increase the number of rays traced in the radiant heat transfer algorithm and found that doubling the number of rays in both directions only changed the total heat transfer by 0.2% (with the other parameters left constant). Thus, for the radiation analysis, we used four separate θ and ϕ divisions in all the final simulations.

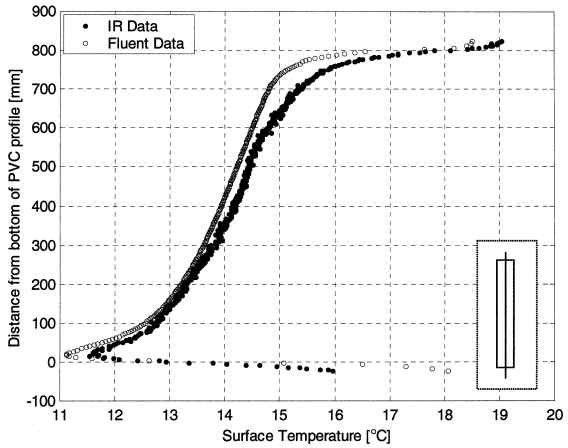

Figure 7 *Surface temperature of vertical, two-inch cavity; experimental uncertainty is estimated to ±0.5ºC (Griffith and Arasteh 1999).*

For high-aspect-ratio cavities such as those typically found in glazing, it is known that secondary (multicellular) flow can exist (see, e.g., Zhao et al. 1997 or Wright and Sullivan 1994). Therefore, we first wanted to check whether the CFD program was capable of simulating such a flow even though secondary flow does not necessarily exist for cavities with a low width (W) to length (L) aspect ratio. In Table 1 we see that the vertical aspect ratio of our samples ranges from approximately 17 to 37 and that the Rayleigh number can be within the multicellular regime (Zhao et al. 1997). Two different two-dimensional cases were tested, one cavity with an aspect ratio of 20 and another with an aspect ratio of 40. Both were simulated with a Rayleigh number of 10^4, known to produce secondary flow. Multicellular flow resulted in both cases. The Nusselt numbers $Nu_{A=20} = 1.404$ and $Nu_{A=40} = 1.256$ were also close to what other investigators have found. ElSherbiny et al. (1982) found 1.404 and 1.240, respectively. In our simulations, the cavity had two isothermal sidewalls separated by two horizontal adiabatic walls.

RESULTS

The data from our experiments and simulations can be presented in several ways. Here we look at both the temperature along vertical lines and the surface temperature in two-dimensional contour plots. The different line plot figures include schematics of the locations on the samples where the temperature data were collected. The absolute uncertainties in the measured data for Figures 7 through 12 are estimated to be

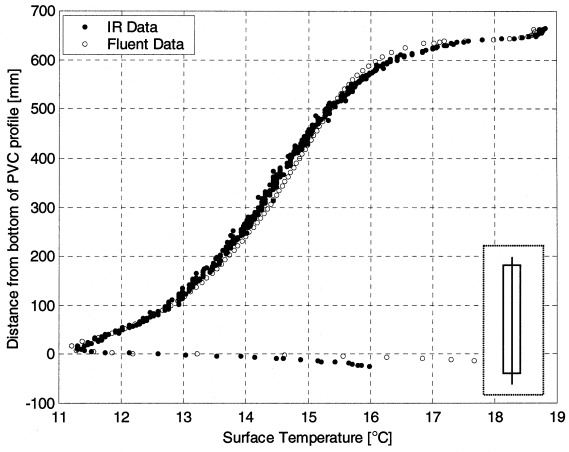

Figure 8 *Surface temperature of the vertical, two-inch H-section; experimental uncertainty is estimated to ±0.5ºC (Griffith and Arasteh 1999).*

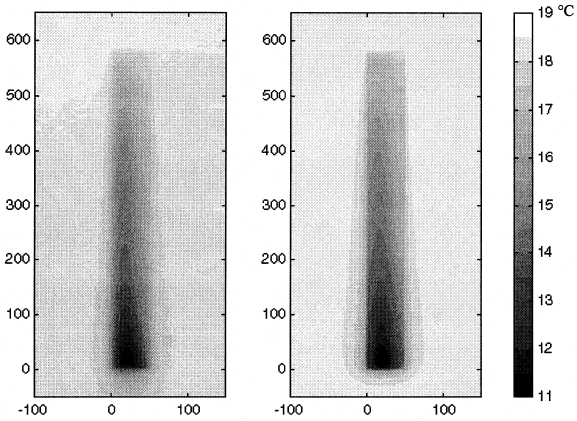

Figure 9 *Contour plot of surface temperature for the two-inch U-section mounted vertically with the open side on the left. The plot on the left is from infrared measurements, and the plot on the right is from CFD simulations. The units for the horizontal and vertical axes are both millimeters. Experimental uncertainty is estimated to ±0.5ºC (Griffith and Arasteh 1999).*

±0.5°C for temperature and ±3 mm for the distance. Table 4 shows the number of nodes, number of iterations, and final residuals for each simulated case. Additional details related to each case are noted below.

Line Plots of Surface Temperature

Figure 7 shows the surface temperature along a line down the middle of the vertical, two-inch cavity. The vertical axis shows the distance from the bottom of the profile; 0 mm is at the bottom of the profile, and 800 mm is at the top. Above and below the specimen, data are plotted for the temperature of the foam surround panel in which the frame section was mounted.

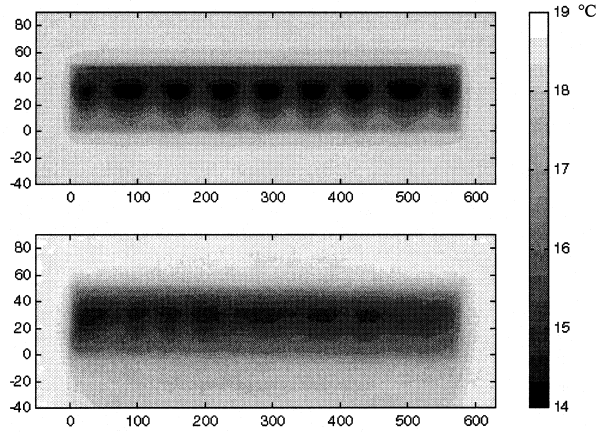

Figure 10 *Surface temperature of the two-inch U-section mounted horizontally with the open side on the top; the top plot is from simulations, and the bottom is measured. Experimental uncertainty is estimated to ±0.5ºC (Griffith and Arasteh 1999).*

The horizontal axis shows the surface temperature in °C. The IR data were determined by averaging some data points on each vertical level to reduce the noise level in the data. However, because the temperature varies in the horizontal direction, the number of data points averaged were kept to a minimum (about 3 data points, equal to a length of approximate 5 millimeters). For the CFD simulation, a symmetry boundary condition was used along the middle of the PVC section.

Figure 8 shows the temperature of the middle part of the 640-mm-long 2-inch H-section mounted vertically. The horizontal axis shows the temperature in ºC, and the vertical axis shows the location on the specimen surface in millimeters. The coordinate 0 is set to be at the bottom of the section. A symmetry boundary condition was used in the numerical simulation.

Contour Plots of Surface Temperature

In Figure 9 we see contour plots of the surface temperature of the vertical, two-inch U-section shown to the right in Figure 1. The 580-mm-long profile was mounted vertically with the open part to the left. The vertical axis shows the accumulated distance from the bottom of the profile and the horizontal axis the distance from the left edge of the specimen. The units on both axes are millimeters. The plot to the left shows thermography results, and the plot to the right shows CFD results. The separate bar to the right shows the relation between gray scale and temperature in ºC. In the numerical simulations for these sections, the scaled energy residuals did not decrease to 10^{-6} but stopped at 7×10^{-6}. However, we still assume a converged solution because the heat transfer through the specimen converged to a constant level.

In Figure 10 we see the results for the same section described above but this time horizontally mounted with the

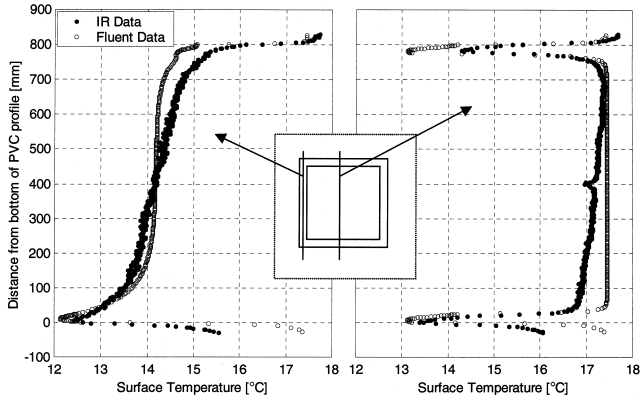

Figure 11 *Surface temperature of the one-inch square frame; the left graphs show the temperature along the middle of the vertical part of the complete frame. The right graphs show the temperature along a vertical line down the middle of the frame. Experimental uncertainty is estimated to ±0.5ºC (Griffith and Arasteh 1999).*

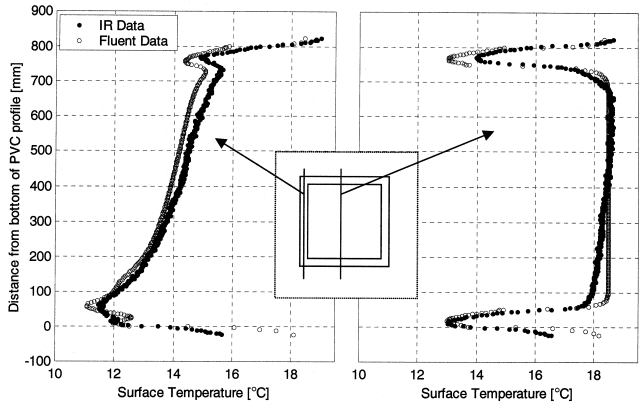

Figure 12 *Surface temperature of the two-inch square frame; the left graphs show the temperature along the middle of the vertical part of the complete frame. The right graphs show the temperature along a vertical line down the middle of the frame. Experimental uncertainty is estimated to ±0.5ºC (Griffith and Arasteh 1999).*

open part of the cavity on the top. The dimensions on both axes are millimeters, and the lower-left corner of the specimen has the coordinate (0,0). In the CFD simulation for this test specimen, we found that the residuals oscillated somewhat. That is, the energy residual reduced to 7×10^{-6}, continuity to 1.5×10^{-4}, and the scaled x-, y-, and z-velocity residuals to less than 5×10^{-5}. The total heat flux through the test specimen and the XEPS panel varied between 11.7 and 11.9 W/m^2-K. Because no transient studies were conducted in the experimental part of this work, we did not pursue a transient numerical solution either (at this stage). The results were still included to show that such a flow pattern can exist within horizontal window frame geometries.

The One-Inch and Two-Inch Square Frames

Figures 11 and 12 show the temperature along different lines on the warm surfaces of the one-inch and two-inch square frames, respectively. In both the figures, the left graphs show the temperature along the middle of the vertical part of the complete frame. The graphs to the right show the temperature along a vertical line down the middle of the frames. The horizontal axis shows the temperature in ºC, and the vertical axis shows the distance from the bottom of the frame in millimeters. Symmetry boundary conditions were used for both sections. We had problems finding a converged solution for the two-inch square frame. After switching to a transient solution procedure, we found that the warm-side surface temperature in the bottom corner not did change more than 0.01°C, well within the uncertainty range of our experiments. The air temperature inside the cavity, in the bottom corner, oscillated between 4.64°C and 5.28°C. The heat flux through the frame seemed to converge against 46.56 W/m^2.

DISCUSSION

Surface Temperature of Frame Sections

Both for the vertical, two-inch cavity, Figure 7, and the vertical, two-inch H-section, Figure 8, we see that there is good agreement between the results from the simulations and the experiments. Except for at the XEPS foam panel, the difference is less than the 0.5°C uncertainty in the infrared measurements. For the foam panel we see that the CFD program predicts lower temperatures at the top than we found in the experiments. The most likely reason for this is that the foam panel over the test specimen does not have as low a temperature as required to create as high a convective heat-transfer coefficient as used in the simulations. Thus, at the top, the total heat-transfer coefficient for the foam is less in the experiment than in the simulation. However, below the test specimen, the situation is the opposite. We see that the temperature measured in the experiment is lower than the temperature generated by the simulation. This phenomenon is generally expected, arising from the use of fixed surface heat-transfer coefficients, although, in reality, the convective portion of the total varies locally.

We also find good agreement between the measured and calculated temperatures for the vertical two-inch U-section shown in Figure 9. Just as for the cases discussed above, we find that the biggest difference is between the temperatures on the XEPS foam panel below the sample.

Both the experimental and simulation results show an interesting and complex surface temperature pattern for the horizontal two-inch U-section (Figure 10). There appears to be a multicellular flow that the CFD simulation has done a fairly good job of predicting, as shown by the fairly good agreement in the scale and number of airflow cells. There are three possible reasons for the difference between the numerical simulations and the IR thermography results. The first reason might be that there are differences between the simulated and the measured profile; the measured section had rounded corners and did not have perfectly equal dimensions throughout the length of the section. The second reason for the difference between the simulated and measured section might be transient behavior, and the third reason might be that the boundary conditions were different.

Surface Temperature of One-Inch and Two-Inch Square Frame

There is more discrepancy between the measured data and the numerical data for the four-sided frames than for the other sections, especially for the upper part of the frames and for the foam insert. The experimental results show that the surface temperature of the foam insert decreases with decreasing distance from the bottom edge (valid for both frames). This is probably a result of variation in surface heat-transfer coefficient with height. An inconstant heat-transfer coefficient is probably also the reason for the temperature difference between the experimental and simulation results for the upper part of the frames. However, for the rest of the specimens, the agreement between the experimental and simulated results is good.

CONCLUSION

We conclude that conjugate CFD simulations are useful for evaluating natural convection heat transfer in frame cavities. The CFD program was able to model combined natural convection and heat transfer well enough for generally good agreement between simulated and measured surface-temperature results. Results for all three vertical cavity cases agreed within the measurement uncertainty. The horizontal U-section specimen displayed a complex multicellular flow; although some discrepancies between the measured results and the numerical simulations can be found, the simulation was able to produce a qualitative temperature pattern that matches the measurements. The four-sided frames showed the largest deviations between measurements and simulations.

Based on this work, we conclude that CFD simulations can be used to study convection effects in the internal cavities of window frames. To further increase the accuracy of these simulations, fluid flow would need to be simulated at the warm-side and cold-side surfaces of the frame sections. However, for the moment, because of the computer resources that such three-dimensional problems require, simulating both external and internal flows will likely be limited to two-dimensional models, especially for the complex realistic geometries found in real window frames.

Future research will study these and additional CFD results in more detail, seeking more insight into the convection effects that arise in complete window frames in contrast to those found in single vertical and horizontal cavities. A study of ways in which the conductive heat-transfer software tools in use today can be used to calculate the thermal performance of window frames with reasonable accuracy will also be performed.

ACKNOWLEDGMENTS

This work was supported by Hydro Aluminum and the Assistant Secretary for Energy Efficiency and Renewable Energy, Office of Building Technology, State and Community Programs, Office of Building Systems of the U.S. Department of Energy under Contract No. DE-AC03-76SF00098.

REFERENCES

ASTM 1199. *ASTM C 1199, Standard test method for measuring the steady state thermal transmittance of fenestration systems using hot box methods*. Annual Book of ASTM Standards, Vol. 04.06. Philadelphia: American Society for Testing and Materials.

Bales. 1993. *The BSI TIP, Thermal image processor, Operator's manual.* Bales Scientific Inc., Walnut Creek Calif., USA.

Carpenter, S.C., and A.H. Elmahdy. 1994. Thermal performance of complex fenestration systems. *ASHRAE Transactions* 100(2):1179-1186.

Carpenter, S.C., and A. McGowan. 1998. Three-dimensional heat transfer effects in building components. *ASHRAE Transactions* 104(1B):1070-1076.

CEN. 1998. *prEN ISO 10077-2, Thermal performance of windows, doors and shutters—Calculation of thermal transmittance—Part 2: Numerical method for frames*. Brussels: European Committee for Standardization.

ElSherbiny, S.M., G.D. Raithby, and K.G.T. Hollands. 1982. Heat transfer by natural convection across vertical and inclined air layers. *Journal of Heat Transfer Transactions of the ASME* 104:96-102.

EE (Enermodal Engineering). 1995. *FRAMEplus toolkit, version 4.0*. Kitchener, Ontario: Enermodal Engineering.

Finlayson, E., R. Mitchell, D. Arasteh, C. Huizenga, and D. Curcija. 1998. *THERM 2.0: Program description. A PC program for analyzing the two-dimensional heat transfer through building products*. Berkeley, California: University of California.

Fluent. 1998. *FLUENT 5 User's Guide*. Fluent Incorporated, Lebanon, U.K.

Griffith, B.T., and D. Arasteh. 1999. Buildings research using infrared imaging radiometers with laboratory thermal chambers. In *Proceedings of the thermosense XXI conference* (D.H. LeMieux, J.R. Snell, eds.). Vol. 3700:

502-513. The International Society for Optical Engineering.

Griffith, B., D. Curcija, D. Türler, and D. Arasteh. 1998. Improving computer simulations of heat transfer for projecting fenesration products: Using radiation view-factor models. *ASHRAE Transactions* 104(1B):845-855.

Griffith, B.T., F. Beck, D. Arasteh, and D. Türler. 1995. Issues associated with the use of infrared thermography for experimental testing of insulated systems. In *Thermal performance of the exterior envelopes of buildings VI*. Atlanta: American Society of Heating, Refrigerating and Air-Conditioning Engineers.

ISO. 1994. *Thermal insulation—Determination of steady-state thermal transmission properties—Calibrated and guarded hot box*. Geneva: International Organisation for Standardisation.

ISO. 1998. *Thermal performance of doors and windows—Determination of thermal transmittance by hot box method*. Geneva: International Organisation for Standardisation.

Larsson, U., B. Moshfegh,and M. Sandberg. 1999. Thermal analysis of super insulated windows (numerical and experimental investigations). *Energy and Buildings* 29: 121-128.

Patankar, S.V. 1980. *Numerical heat transfer and fluid flow.* Washington, D.C.: Hemisphere.

Shewen, E., K.G.T. Hollands, and G.D. Raithby. 1996. Heat transfer by natural convection across a vertical air cavity of large aspect ratio. *Journal of Heat Transfer Transactions of the ASME* 118:993-995.

Sullivan, H.F., J.L. Wright, and R.A. Fraser. 1996. Overview of a project to determine the surface temperatures of insulated glazing units: Thermographic measurement and two-dimensional simulation. *ASHRAE Transactions* 102(2):516-522.

Türler, D., B.T. Griffith, and D. Arasteh. 1997. Laboratory procedures for using infrared thermography to validate heat transfer models. In *Insulation materials: Testing and applications*, third volume, ASTM STP 1320 (R.S. Graves, R.R. Zarr, eds.). Philadelphia: American Society for Testing and Materials.

Wright, J.L., and H.G. Sullivan. 1994. A two-dimensional numerical model for natural convection in a vertical, rectangular window cavity. *ASHRAE Transactions* 100(2):1193-1206.

Yin, S.H., T.Y. Wung, and K. Chen. 1978. Natural convection in an air layer enclosed within rectangular cavities. *International Journal of Heat and Mass Transfer* 21:307-315.

Zhao, Y., D. Curcija, and W.P. Goss. 1997. Prediction of the multicellular flow regime of natural convection in fenestration glazing cavities. *ASHRAE Transactions* 103(1):1009-1020.